Received: 30 October 2023 | Revised: 25 January 2024 | Accepted: 4 March 2024

DOI: 10.1002/htj.23044

ORIGINAL ARTICLE

HEAT TRANSFER WILEY

Heat transfer assessment incorporated with entropy generation within a curved corner structure enclosing a cold domain

Jiaul Haque Saboj[1,2] | **Preetom Nag**[1,2] | **Goutam Saha**[3,4] | **Suvash C. Saha**[4]

[1]Department of Mathematics & Physics, North South University (NSU), Dhaka, Bangladesh

[2]Center of Applied & Computational Sciences (CACS), NSU, Dhaka, Bangladesh

[3]Department of Mathematics, University of Dhaka, Dhaka, Bangladesh

[4]School of Mechanical and Mechatronic Engineering, University of Technology Sydney, Ultimo, New South Wales, Australia

Correspondence
Suvash C. Saha, School of Mechanical and Mechatronic Engineering, University of Technology Sydney, Ultimo, NSW 2007, Australia.
Email: suvash.saha@uts.edu.au

Funding information
NSU CTRG, Grant/Award Number: CTRG-22-SEPS-22; The Ministry of Science and Technology (MOST), Government of the People's Republic of Bangladesh, Grant/Award Number: SRG-236670

Abstract

In cold climates or winter countries, maintaining optimal room temperatures is essential for comfort and energy efficiency. Conventional square or rectangle-shaped rooms often face challenges in achieving efficient heat transfer (HT) and uniform temperature distribution. To address these limitations, this study has been explored using curved corner cavities, varying their aspect ratio ($AR = 1.0$ and 0.5), and incorporating a circular shape cooler to enhance HT within the room. The curved corners promote better airflow circulation, creating a more efficient HT environment. The dimensionless governing equations and corresponding boundary conditions are solved numerically using the finite element method. This research aims to assess the optimized HT and entropy production within a curved corner cavity, varying their AR and enclosing a circular shape cooler to determine the most effective configuration for maximizing HT and energy efficiency in winter conditions. This study reveals that in the case without a cooler (WOC), the average Nusselt number (Nu_{avg}) is higher in the curved rectangle cavity compared with the curved

square cavity for all *Ra* values. Using the curved square ($AR = 1.0$), Nu_{avg} increases by 191.86%, while with the curved rectangle ($AR = 0.5$), Nu_{avg} increases by 302.63% at $Ra = 10^6$. Additionally, in the case with a cooler (WC), Nu_{avg} is higher than the case WOC and Nu_{avg}, and an average total entropy (En_{avg}) increases for both the WOC and WC cases for all *Ra* values. Transitioning from a square to a curved rectangle ($AR = 0.5$) WC, Nu_{avg} increases by 329.34% at $Ra = 10^6$. Furthermore, in the WOC case, the curved square cavity and, in the WC case, the curved rectangle show better energy efficiency and reduce environmental impact.

KEYWORDS

curve corner, entropy generation, finite element method, heat transfer, Rayleigh number

1 | INTRODUCTION

In the 21st century, designing buildings in cold climates often involves the prevalent use of sharp, angular corners. Traditional square, rectangular, or irregularly shaped rooms face challenges in achieving efficient heat transfer (HT). Some countries have significantly changed by using curved corners to improve HT. However, this architectural feature is not widely adopted in building design.

Researchers have explored various thermal conditions, including scenarios where the temperature gradient is applied horizontally, as observed in different studies.[1–4] The case of vertical temperature gradients was investigated by Hyun and Lee,[5] McBain,[6] and Ha and Jung.[7] They noticed that average Nusselt number (Nu_{avg}) increased as the Rayleigh number (*Ra*increased. Also, Cheikh et al.[8] numerically explored the natural convection (NC) in a two-dimensional (2D) air-filled square cavity, where the top is cooled, and the bottom is heated continuously under various thermal boundary conditions. They examined various thermal conditions at the upper and side walls and found that Nu_{avg} increased as *Ra* increased for all thermal boundary conditions. Some relevant literature can be found in many studies.[9–15] The research by Natarajan et al.[16] focused on the NC flow within a trapezoidal cavity. They noted that the total HT rate at the lower wall is notably higher when the left wall is subjected to linear heating while the right wall is actively cooled. This suggests that the specific arrangement of wall temperatures impacts HT within the cavity. Corvaro and Paroncini[17] conducted a combined numerical and experimental investigation into NC within an air-filled square cavity. Their experimental findings demonstrated that the *Nu* and velocity values increased with increasing *Ra* numbers. This indicates improved natural convective HT at higher *Ra* numbers. Varol et al.[18] conducted research on the NC inside a right-angle inclined cavity with an inner square body. Their study findings indicated that as *Ra* increased, a greater quantity of streamlines became apparent, and alterations in the isothermal distribution within the

enclosure. After that, Hussein and Hussain[19] explored another study examining the effect of inclination, length of the heater, and Prandtl number (*Pr*) within a regular square cavity, with the heater positioned at a corner surrounded by insulated walls. Their research found that the HT coefficient could either increase or decrease with changes in inclination, but *Pr* had a notable impact on the rate of HT. Saglam et al.[20] conducted both practical experiments and numerical analyses to study NC within a rectangular cavity, specifically focusing on the presence of multiple discrete heat sources, with all heat sources positioned along a hot sidewall. This research emphasized the significance of heat dissipation rates as a critical factor in improving the cooling effectiveness of heat emitters. Rabani[21] investigated the impact of different chord shapes and variations in the *Ra* on HT inside a triangular cavity. It is found that changing the shape of the cavity, especially with an area reduction, results in a decrease in the *Nu* and, consequently, a decrease in HT. This indicated that HT is influenced by the deformation of the lower wall of the cavity. Saleem and Alshara[22] focused on a numerical examination of NC flow in a triangular cavity exposed to a cold air stream from both side walls. They found that the AR influences HT, with an 83% increase as AR goes from 0.25 to 1. Alipanah et al.[23] investigated the impact of adding ultrafine metallic nanoparticles to a pure fluid on entropy generation within a square cavity, employing the second law of thermodynamics. They found that as *Ra* increased, the efficiency of nanoparticle addition decreased in reducing entropy generation (EG).

Natural convection studies within cavities featuring an inner circular cylinder have been a prominent area of research over the past few decades, resulting in numerous archived publications. Numerous investigations have explored the influence of diverse forms and dimensions of internal structures on NC in enclosures.[24–26] Kim et al.[27] explored the geometry of a square cavity, specifically focusing on how the vertical positioning of a cylinder inside the cavity affected the flow patterns. Their observations uncovered that the quantity, dimensions, and configuration of flow cells within the cavity are notably affected by both *Ra* and the placement of the inner circular cylinder. Chowdhury et al.[28] conducted an investigation of NC flow inside a triangular cavity with the existence of a circular heated body. Their findings indicated that changes in the HT rate and the circular body's radius have a substantial influence on the flow patterns and temperature distribution within the triangular cavity. In a study by Ali et al.,[29] they examined NC flow in a shallow water-filled square cavity. Their results demonstrated that Nu_{avg} rose with an increase in *Ra*. Additionally, the study identified a region of overlap between the two aspect ratios (ARs), suggesting a range of conditions where both ARs exhibit similar HT behavior. Welhezi et al.[30] observed a significant increase in HT with rising *Ra* in a 3D numerical simulation conducted to investigate NC phenomena occurring between an inner hot cube and its outer spherical cavity. Recently, Saboj et al.[31] conducted a study that analyzed the HT and EG within an octagonal cavity containing a cold cylindrical body. They found that including an inner cold cylinder in the octagonal cavity increased the Nu_{avg} and EG. A separate set of investigations has been carried out to explore how the insertion of fins affects the performance of NC within cavities. Arquis and Rady[32] conducted a study to examine flow and HT characteristics in a horizontal fluid layer featuring fin attachments on the lower surface. Their investigation focused on how HT and fluid flow were influenced by variations in fin height and the gaps between fins. Dou et al.[33] explored HT in a cavity equipped with a fin array. The researchers investigated the impact of several fin parameters on HT rates. These parameters include fin height, fin number, and fin shape. Taloub et al.[34] investigated double-diffusive NC within an annulus area formed by two horizontal confocal elliptical solids. They observed that increasing the thermal *Ra* results in higher values for both Nu_{avg} and Sh_{avg}.

Khan et al.[35] investigated the convective HT characteristics of an $_{Al2}O_3$–Cu–H_2O hybrid nanofluid inside a triangular fin-shaped cavity. They found that both local and Nu_{avg} show an increasing trend with higher Ra.

Biswas et al.[36] investigated the complex triple-convective flow physics of a magnetically susceptible fluid containing copper nanoparticles and oxytactic bacteria in a unique W-shaped porous cavity. They revealed that Nu_{avg} and Sh_{avg} for the W-shaped cavity are higher compared with square and trapezoidal cavities. Mandal et al.[37] delved into mixed magneto-thermal convection in a W-shaped enclosure filled with Cu–Al_2O_3–H_2O hybrid nanofluid saturated in a porous structure. The study revealed that an increase in the side inclination angle deteriorates HT despite having the same heating length. This study also revealed that Hartmann number (Ha) suppresses flow velocity, resulting in a drop in Nu. After that, Mandal et al.[38] focused on the magnetohydrodynamic (MHD) thermofluidic transport process within an innovative M-shaped cavity filled with permeable materials and Al_2O_3–Cu hybrid nanoparticles suspended in H_2O. They also found that a decrease in Da or Ha values results in a drop in flow strength and, consequently, a decrease in HT. Later on, Mandal et al.[39] investigated the MHD mixed bioconvection with oxytactic microorganisms suspended in Cu–H_2O nanofluid. They found that the presence of undulating curved surfaces enhanced HT up to certain optimal magnitudes of undulations under different operating conditions. This suggested that the geometry of the wavy sidewall plays a crucial role in HT enhancement. Al-Farhany et al.[40] focus on investigating double-diffusive NC in a complex cavity containing two equilateral triangular obstacles. They found that as Ra increased, both Nu_{avg} and Sh_{avg} increased.

The practical implication of the considered problem lies in its potential to enhance the design and efficiency of thermal systems. By investigating HT and EG within curved corner enclosures, our study offers insights that can be applied to real-world scenarios. Practical implications include optimizing the thermal performance of spaces with unconventional geometries, leading to improved energy efficiency and more effective temperature regulation. This research may find applications in diverse fields, such as building design, HVAC systems, and industrial processes, contributing to the development of more efficient and sustainable technologies. The author's expertise, along with existing literature, underscores the importance of investigating HT and EG within confined systems as they relate to real-world applications. The present investigation aims to recognize the potential benefits of this architectural innovation and to help in more effective building designs in the future. This study's novelty is its specific focus on analyzing HT and EG within curved corner cavities, varying their ARs, and enclosing a circular shape cooler. While previous research has examined HT in various cavity shapes like squares and rectangles, the study of HT and EG in this distinctly curved corner geometry has yet to be undertaken. This distinctive geometry introduces new and unique HT characteristics and EG mechanisms within the cavity.

2 | FORMULATION OF THE PROBLEM

2.1 | Physical model

This study introduces a novel approach to improve HT and achieve more uniform temperature distribution in conventional square or rectangle-shaped rooms. This study delves into using curved corner cavities with an inner cooling system for $AR = 1$ and 0.5 to enhance HT within the room. While not all results are presented here, our exploration consistently demonstrated

higher HT rates within curved corner cavities than square or rectangular ones. Furthermore, incorporating a circular cylinder has yielded even more significant enhancements in HT rates. This innovative physical model, as depicted in Figure 1, offers promising potential for addressing the challenges associated with conventional room heating and cooling systems.

Figure 1A illustrates a curved square enclosure with an inner cooler of radius $0.15L$. The cooler, along with the upper and lower horizontal surfaces, is held at a low temperature (T_c), while the bottom-left and top-right curve heated walls sustain a constant heat flux. The bottom-left and top-right heat flux walls are $0.57L$, and the two vertical walls are adiabatic, with a length of $0.6L$. For $AR = 1.0$ and 0.5, the cold walls have a length of $0.6L$ and $1.6L$, respectively. The fluid considered is air with a temperature of 20°C and a Pr of 0.72. Figure 1B illustrates the mesh schematics. A nonuniform triangular mesh is employed in this study, with increased density near the walls. The fluid flow being examined is presumed to be steady, 2D, incompressible, laminar, and Newtonian. Internal and external magnetic forces, viscous dissipation, and radiation effects are considered negligible. The interactions between fluid particles and nanoparticles are neglected due to the absence of nanoparticles.

2.2 | Mathematical modeling

The dimensionless governing equations for continuity, momentum, and energy for a 2D, steady, laminar, and incompressible flow with the Boussinesq approximation can be expressed as follows[41]:

$$\frac{\partial U}{\partial X} + \frac{\partial V}{\partial Y} = 0, \tag{1}$$

$$U\frac{\partial U}{\partial X} + V\frac{\partial U}{\partial Y} = -\frac{\partial P}{\partial X} + Pr\left[\frac{\partial^2 U}{\partial X^2} + \frac{\partial^2 U}{\partial Y^2}\right], \tag{2}$$

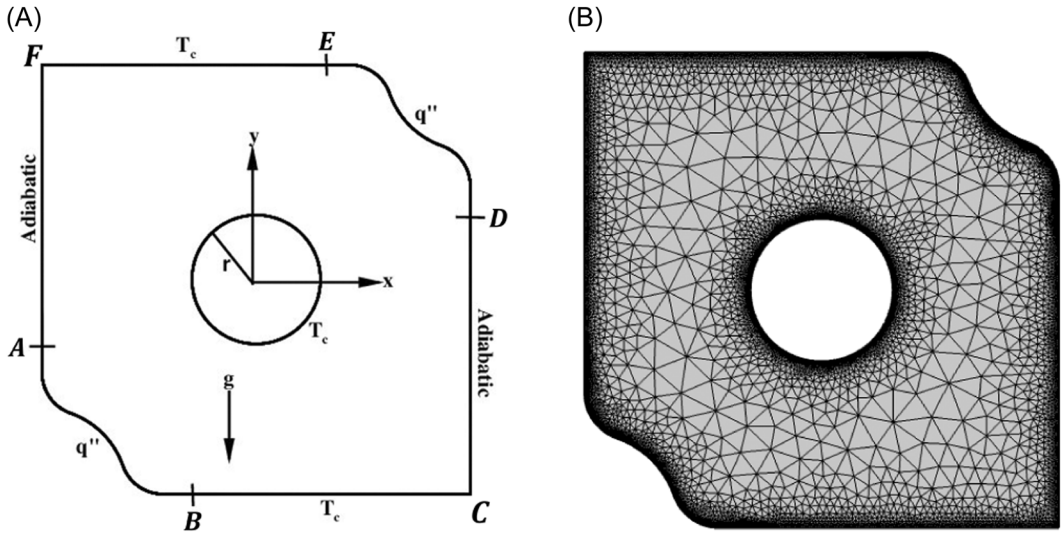

FIGURE 1 (A) Illustration portraying the model configuration and (B) schematics of mesh.

$$U\frac{\partial U}{\partial X}+V\frac{\partial U}{\partial Y}=-\frac{\partial P}{\partial X}+Pr\left[\frac{\partial^2 U}{\partial X^2}+\frac{\partial^2 U}{\partial Y^2}\right]+RaPr\Theta, \tag{3}$$

$$U\frac{\partial \Theta}{\partial X}+V\frac{\partial \Theta}{\partial Y}=\left(\frac{\partial^2 \Theta}{\partial X^2}+\frac{\partial^2 \Theta}{\partial Y^2}\right). \tag{4}$$

The following nondimensional quantities are utilized to develop Equations (1)–(4).[31]

$$\begin{aligned} &X=\frac{x}{L},\quad Y=\frac{y}{L},\quad U=\frac{uL}{\alpha},\quad V=\frac{vL}{\alpha},\quad Ra=\frac{gL^4\beta\rho q''}{\alpha k\mu},\\ &Pr=\frac{\nu}{\alpha},\quad P=\frac{pL^2}{\rho\alpha^2},\quad \Theta=\frac{(T-T_{ref})k}{q''L}. \end{aligned} \tag{5}$$

Boundary conditions

- All walls: $U=V=0$.
- Horizontal walls BC and EF: $\Theta=0$.
- Vertical walls CD and AF: $\frac{\partial \Theta}{\partial X}=0$.
- Cooler surfaces: $\Theta=0$.
- Curved walls (CWs) AB and DE: $q''=-1$.

The local Nusselt number (Nu) helps us understand how much heat is being transferred in the system from the active walls. In this manner, the average quantity for HT rate is evaluated by the average Nusselt number (Nu_{avg}), which is calculated as follows[31]:

$$Nu_{avg}=\frac{1}{l_{cw}}\int_{cw} Nu\,dl,\quad \text{where } Nu=-\frac{1}{\theta_{cw}}, \tag{6}$$

where dl indicates the infinitesimal arc length along the CWs and l_{cw} is the total length of the CWs.

The local total entropy generation is defined as follows[42]:

$$S_{TL}=S_{HT}+S_{FF}, \tag{7}$$

where

$$S_{HT}=\left(\frac{\partial \theta}{\partial X}\right)^2+\left(\frac{\partial \theta}{\partial Y}\right)^2, \tag{8}$$

$$S_{FF}=\lambda\left[2\left(\frac{\partial U}{\partial X}\right)^2+2\left(\frac{\partial V}{\partial Y}\right)^2+\left(\frac{\partial U}{\partial Y}+\frac{\partial V}{\partial X}\right)^2\right]. \tag{9}$$

There is no fixed irreversibility factor. Here the irreversibility factor, $\lambda=\frac{\mu T_0\alpha^2}{kL^2\Delta T}$, is equal to 10^{-4} as Ilis et al.[42] and Sivaraj and Sheremet.[43]

In the equations above, S_{HT} represents the entropy production due to HT, and S_{FF} represents the entropy production due to fluid friction.

The average entropy generation (En_{avg}), local Bejan number (Be), and average Bejan number (Be_{avg}) are defined as[42]

$$En_{avg} = \frac{\int_0^1 \int_0^1 S_{TL}\, dX\, dY}{\int_0^1 \int_0^1 dX\, dY}, \tag{10}$$

$$Be = \frac{S_{HT}}{S_{HT} + S_{FF}}, \tag{11}$$

$$Be_{avg} = \frac{\int_0^1 \int_0^1 Be\, dX\, dY}{\int_0^1 \int_0^1 dX\, dY}. \tag{12}$$

3 | NUMERICAL MODELING AND VALIDATION

The numerical simulations in this study were conducted using the finite element method (FEM), a well-established computational technique for solving complex HT problems. FEM discretizes the curved corner cavity into a mesh of elements, allowing for a detailed representation of the geometry. This approach enables the accurate modeling of HT phenomena and provides a robust foundation for the analysis. In this study, the FEM is utilized to solve the governing equations (1)–(4) and their corresponding boundary conditions. The governing partial differential equations were converted into integral equations using the Galerkin weighted residual technique in this simulation approach. Additionally, a nonuniform triangular mesh was used, and we assessed the accuracy using error criteria with a relative tolerance of 10^{-6}.

3.1 | Grid sensitivity test

To ensure the accuracy and dependability of the simulation, a grid independence test is carried out. This test involves simulating various grid sizes while maintaining all other parameters constant. The objective is to determine the optimal grid size for our study, and we conducted this test using a triangular mesh with five different grid sizes. Table 1 presents a comparison of Nu_{avg} and simulation time (s) for various grid sizes for $AR = 1.0$ and 0.5 at $Ra = 10^6$, where $M_1 = 4618$ and $N_1 = 3864$. The values in the brackets indicate the absolute error percentage of M_4 and N_4 in comparison to others. Following the comparison, a grid size of$8M_1$ was selected for $AR = 1.0$, and $8N_1$ was selected for $AR = 0.5$ to balance computational accuracy and time cost in the simulations.

3.2 | Validation

The streamlines and isotherms for a laminar, incompressible fluid flow within a square cavity subjected to a heated circular cylinder at $Ra = 10^6$ are shown in Figure 2. The outcomes are qualitatively consistent with earlier results published by Kim et al.[27] In addition, Figure 3

TABLE 1 Variation of Nu_{avg} and simulation time for different mesh distribution for $Ra = 10^6$ for $AR = 1.0$ and 0.5.

$AR = 1.0$					
Elements	M_1	$M_2 = 2M_1$	$M_3 = 4M_1$	$M_4 = 8M_1$	$M_5 = 16M_1$
Air ($Pr = 0.72$)	88.79	86.55	87.13	84.56	83.65
	(5.00%)	(2.36%)	(3.05%)	(0%)	(1.08%)
Time (s)	3	4	5	6	10
$AR = 0.5$					
Elements	N_1	$N_2 = 2N_1$	$N_3 = 4N_1$	$N_4 = 8N_1$	$N_5 = 16N_1$
Air ($Pr = 0.72$)	93.21	93.77	92.75	91.32	90.80
	(2.07%)	(2.68%)	(1.56%)	(0%)	(0.57%)
Time (s)	2	3	5	6	9

Abbreviation: AR, aspect ratio.

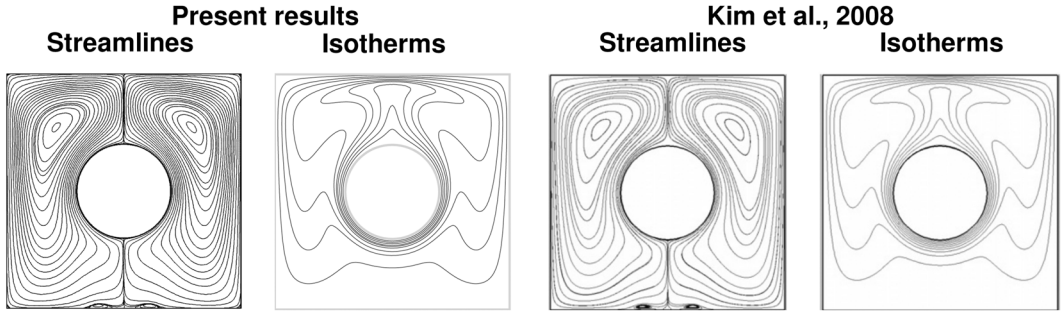

FIGURE 2 Variation of streamlines and isotherms profiles with Kim et al.[27] for $Ra = 10^6$.

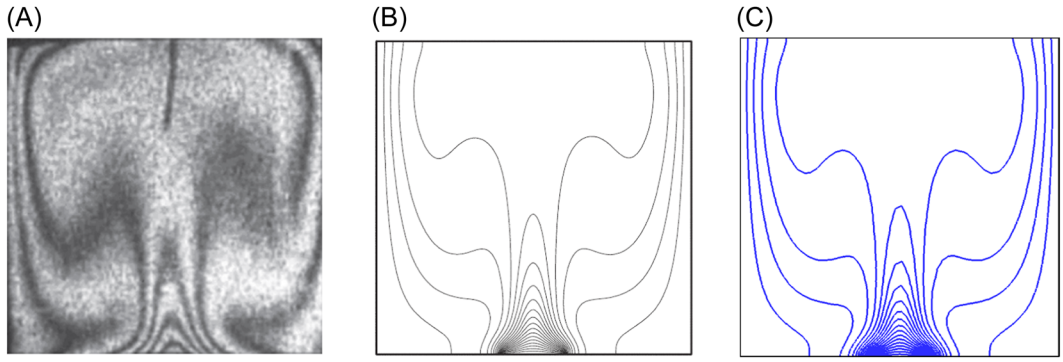

FIGURE 3 Variation of Isotherms profile between the experimental results of Corvaro et al.,[17] Mussa et al.[44] and present results for $Ra = 2.02 \times 10^5$. (A) Corvaro and Paroncini,[17] (B) Mussa et al.,[44] and (C) present results.

shows a comparison of the current isotherm results with the numerical isotherm, as shown in the studies conducted by Mussa et al.,[44] as well as the experimental findings given by Corvaro and Paroncini.[17] This comparison was established through an analysis of an air-filled square cavity heated by a small, localized heat source situated on the bottom wall. The figures provide clear evidence of a significant alignment in the results. To assess the accuracy of the numerical simulation, a comparison of the EG results, including S_{HT}, S_{FF}, and S_{TL} is conducted with the findings published in Ilis et al.[42] for square geometries. The obtained results exhibit excellent agreement, as illustrated in Figure 4. Table 2 presents a comparison of Nu_{avg} between the current findings and those of Kim et al.,[27] indicating good agreement with the previous results. Figure 5 illustrates the alignment between the present results and those of Kim et al.[27] for local Nu at $Ra = 10^4$ and 10^5 over the range of θ from 0° to 180°, providing clear evidence of significant agreement in the results.

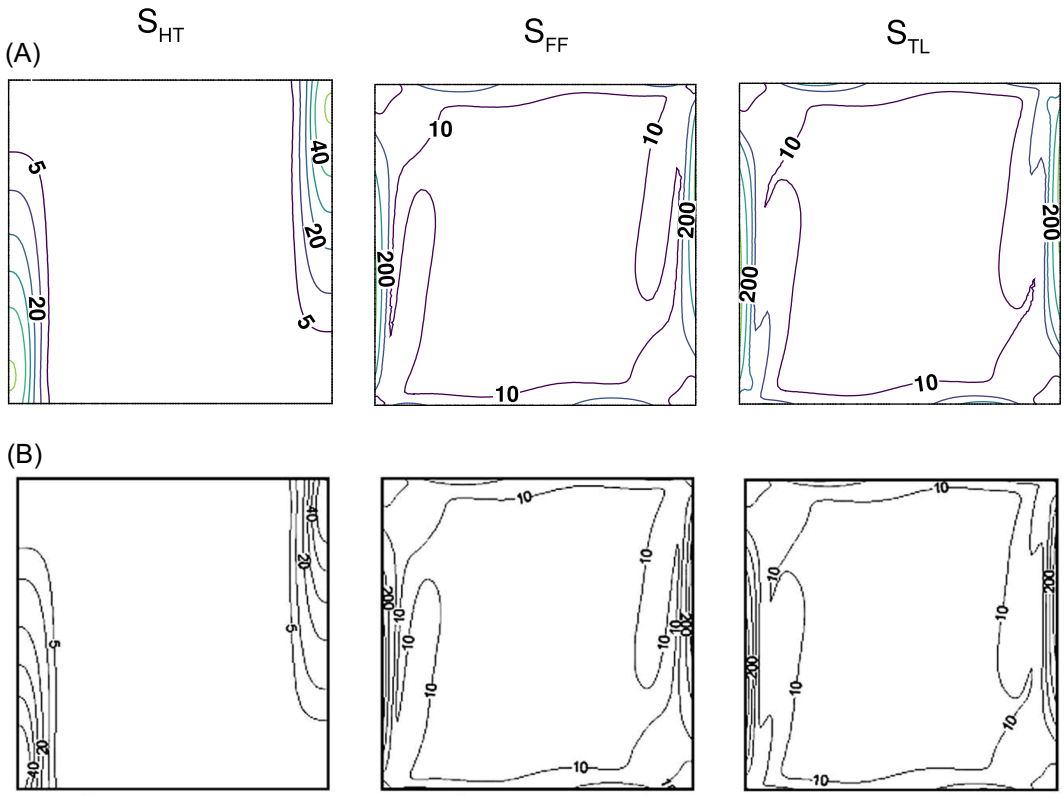

FIGURE 4 Variation of S_{HT}, S_{FF}, and S_{TL} between the results of (A) present results and (B) Ilis et al.[42]

TABLE 2 Comparison of Nu_{avg} between the present results and the results of Kim et al.[27]

Ra	10^3	10^4	10^5	10^6
Present results	5.008	5.062	7.837	14.055
Kim et al.[27]	5.064	5.121	7.766	14.133

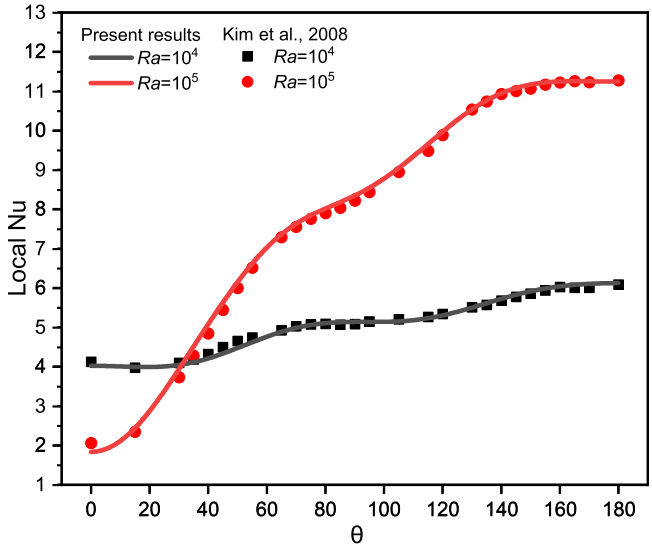

FIGURE 5 Variation of local *Nu* between the results of Kim et al.[27] and present results for $Ra = 10^4$ and 10^5.

4 | RESULTS AND DISCUSSIONS

4.1 | Effects of *Ra* on fluid flow, temperature, and entropy generation

Figure 6 displays the variation of streamlines, isotherms, S_{HT}, S_{FF}, and S_{TL} for *Ra* ranging from 10^3 to 10^6 when $AR = 1.0$. In the streamlines graph, the color gradient represents the velocity magnitude, with red indicating high-velocity magnitude and blue indicating low-velocity magnitude. The black lines in the graph represent the streamlines, showing the paths that fluid particles follow. At $Ra = 10^3$, two prominent vortices are formed near two curved regions. Near the bottom-left curved region, the flow is in a clockwise direction, while near the top-right curved region, the flow is in an anticlockwise direction. As *Ra* increases, the buoyancy force also increases, leading to more pronounced and stronger vortices near the bottom-left curved region. This indicates an increase in fluid circulation in this area. Conversely, the vortices near the top-right curved region tend to weaken and diminish as *Ra* increases. At $Ra = 10^6$, signifying a higher buoyancy force, a new vortex is formed near the top-left corner of the cavity. This suggests a more complex flow behavior in the cavity as *Ra* reaches higher values.

At $Ra = 10^3$, the isotherm contours reveal a nonuniform temperature distribution inside the cavity, with notable temperature variations across different regions. However, the temperature differences between adjacent points in these regions remain relatively small. Interestingly, the isotherms near the two curved regions exhibit closely spaced contours, indicating rapid temperature changes, while those adjacent to the cooler and the bottom wall display flatter contours. As *Ra* increases, signifying a greater buoyancy force, the isotherms near the curved regions become more widely spaced, indicating more pronounced temperature gradients in these areas.

At lower *Ra* values, S_{HT} is dominant over S_{FF}. Figure 6 illustrates that as *Ra* increases, S_{HT} decreases while S_{FF} increases within the cavity. This trend suggests that at higher *Ra* values,

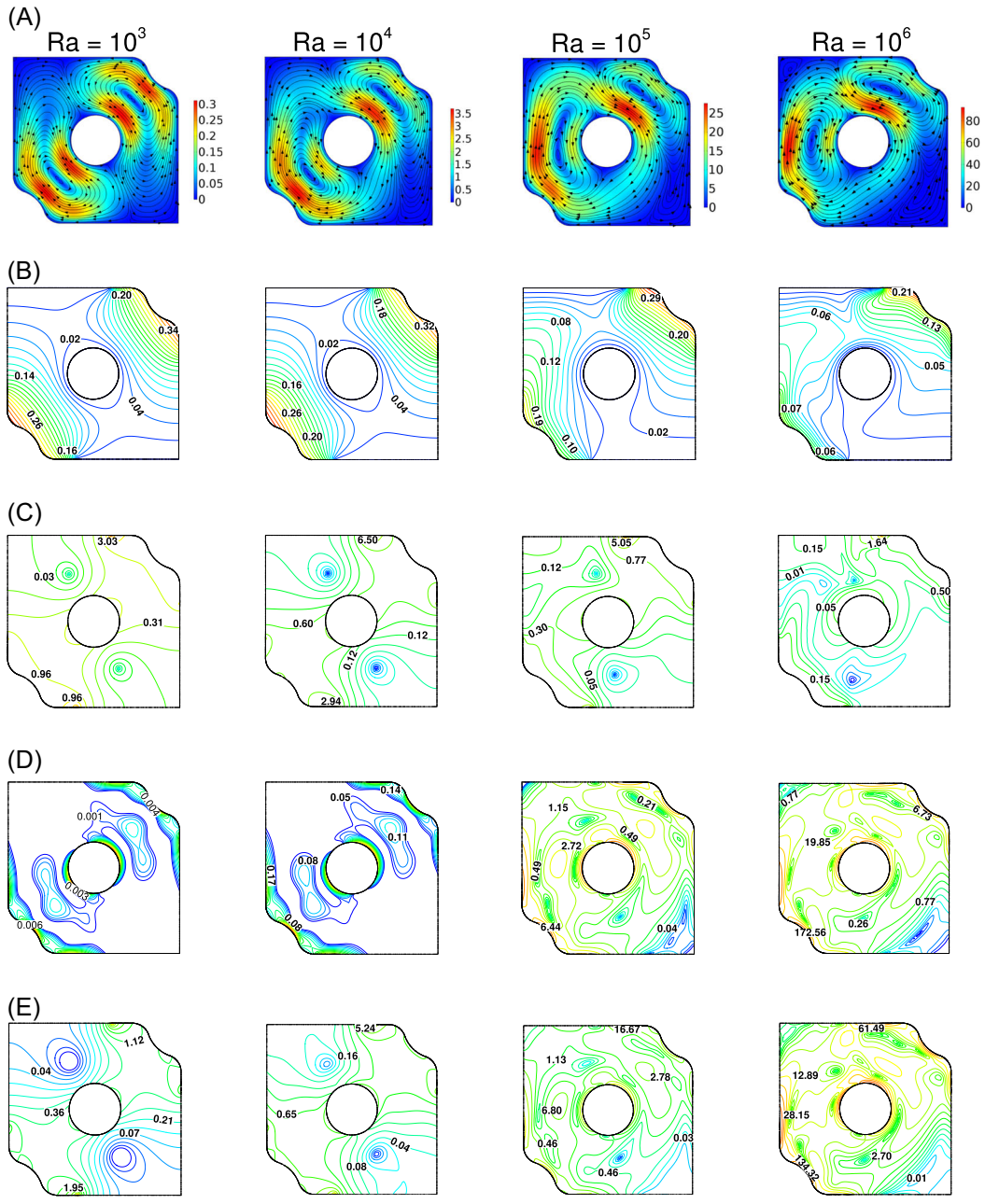

FIGURE 6 Distribution of (A) streamlines, (B) isotherms, (C) S_{HT}, (D) S_{FF}, and (E) S_{TL} for $Ra = 10^3$–10^6 when $AR = 1.0$. AR, aspect ratio.

fluid friction becomes a more significant contributor to EG compared with HT. When *Ra* increases and the buoyancy forces become more robust, fluid motion becomes stronger, increasing fluid friction. The relatively weak buoyancy forces at lower *Ra* result in less fluid motion and weaker fluid friction effects, making HT a dominant factor in generating entropy. Figure 6 also reveals that S_{TL} increases as *Ra* increases. Specifically, regions near the cooler,

where the heat flux wall meets the left adiabatic wall and where the heat flux wall meets the top cold wall, exhibit higher S_{TL} values. This indicates that increasing Ra leads to higher EG associated with thermal losses in these areas.

Figure 7 displays the variation of streamlines, isotherms, S_{HT}, S_{FF}, and S_{TL} for $Ra = 10^4$ and 10^6 when $AR = 0.5$. At $Ra = 10^4$, two prominent vortices form on the left and right sides of the cooler. However, at $Ra = 10^4$, the left vortex exhibits a higher velocity magnitude than the right vortex. Also, it shows that the flow is in a clockwise direction in the left vortex, while in the right vortex, the flow is in an anticlockwise direction. The left vortex becomes more pronounced and stronger as Ra increases. This indicates increased fluid circulation in this area. On the contrary, with the increase in Ra and the associated rise in buoyancy force, the right vortex tends to weaken and diminish. At $Ra = 10^6$, a new vortex is formed near the bottom-right corner of the cavity. This indicates a more intricate flow behavior within the cavity as Ra attains higher values, accompanied by an increase in buoyancy force. The isotherms near the two curved regions exhibit closely spaced contours, indicating rapid temperature changes, while those adjacent to the cooler and the bottom wall display flatter contours. As Ra increases, the contours near the cooler become more pronounced.

At $Ra = 10^4$, S_{HT} is higher than at $Ra = 10^6$ within the cavity, whereas at $Ra = 10^6$, S_{FF} is higher than S_{HT}. This trend suggests that at higher Ra values, fluid friction becomes a more significant contributor to EG compared with HT. As Ra increases and the buoyancy forces become stronger, fluid motion becomes stronger, leading to increased fluid friction and, consequently, higher EG due to fluid friction. Figure 6 also illustrates that S_{TL} increases as Ra increases. Notably, regions near the cooler, where the heat flux wall intersects with the left adiabatic wall and where the heat flux wall intersects with the top cold wall, show higher S_{TL} values. This indicates that increasing Ra results in higher EG associated with thermal losses in these regions.

4.2 | $|V|_{avg}$, Nu_{avg}, average entropy, and Bejan number for different shapes of geometry

Figure 8A,B depicts the changes in the average velocity magnitude ($|V|_{avg}$) for two scenarios: without a cooler (WOC) and with a cooler (WC), across the square, curved square ($AR = 1.0$), and curved rectangle ($AR = 0.5$) cavities as Ra ranges from 10^3 to 10^6. For both scenarios, $|V|_{avg}$ increases with Ra, signifying that higher Ra values correspond to greater $|V|_{avg}$. Notably, in WC cases, $|V|_{avg}$ is lower compared with the WOC case.

Figure 9A,B depicts the variation of Nu_{avg} for two scenarios: WOC and WC, within the square, curved square ($AR = 1.0$), and curved rectangle ($AR = 0.5$) cavities as Ra ranges from 10^3 to 10^6. In both scenarios, Nu_{avg} increases with Ra, indicating that higher Ra values correspond to higher Nu_{avg}. In the square and curve square cavities ($AR = 1.0$), Nu_{avg} is higher in the WC case compared with the WOC case. Interestingly, in the WC case for the curved rectangle cavity ($AR = 0.5$), Nu_{avg} is lower at $Ra = 10^4$, but at $Ra = 10^3$, 10^5, and 10^6, it shows higher Nu_{avg} compared with the WOC case. By employing the curved square ($AR = 1.0$), Nu_{avg} increases by 191.86%, and with the use of the curved rectangle ($AR = 0.5$), Nu_{avg} increases by 302.63% at $Ra = 10^6$. When transitioning from a square to a curved rectangle ($AR = 0.5$) WC, Nu_{avg} increases by 329.34% at $Ra = 10^6$.

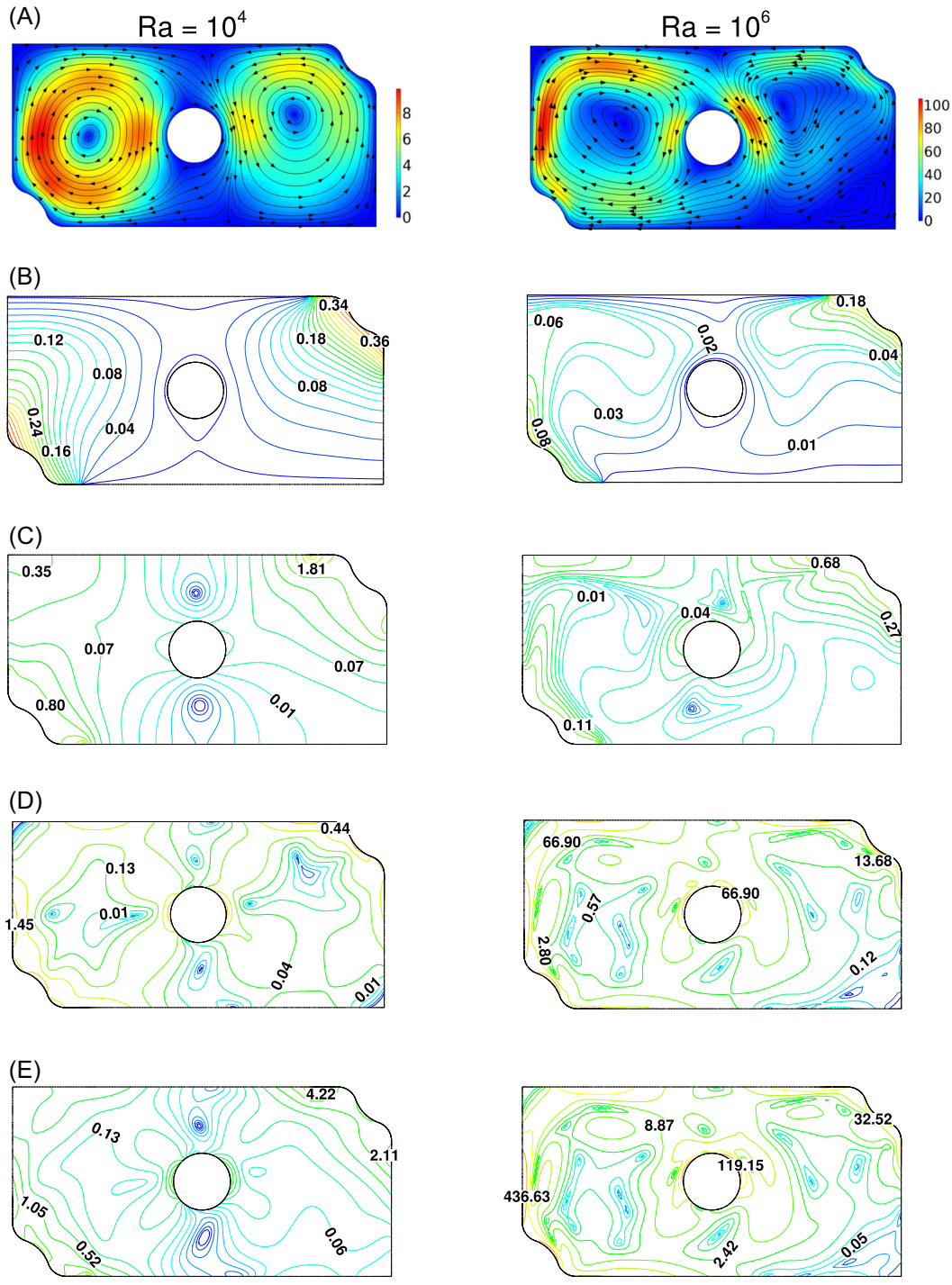

FIGURE 7 Distribution (A) streamlines, (B) isotherms, (C) S_{HT}, (D) S_{FF}, and (E) S_{TL} for $Ra = 10^4$ and 10^6 when $AR = 0.5$.

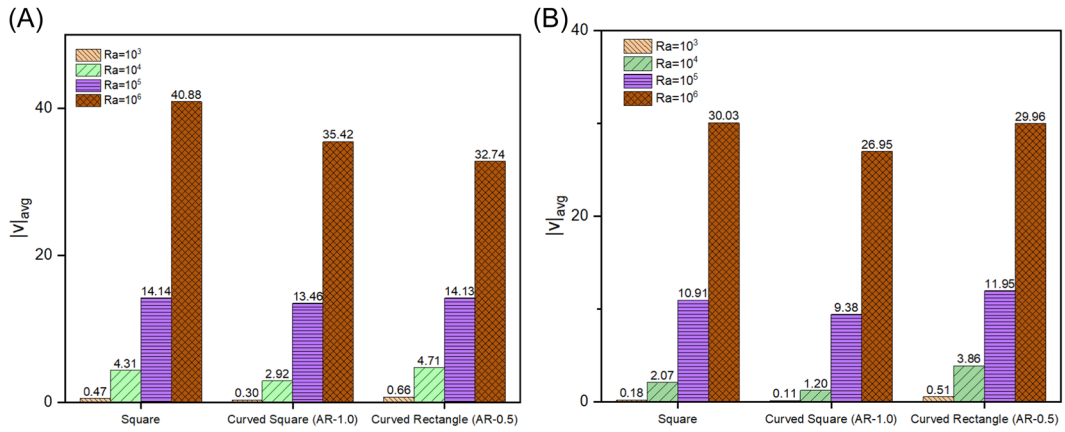

FIGURE 8 Variation of $|v|_{avg}$ (A) without cooler and (B) with cooler for $Ra = 10^3$–10^6.

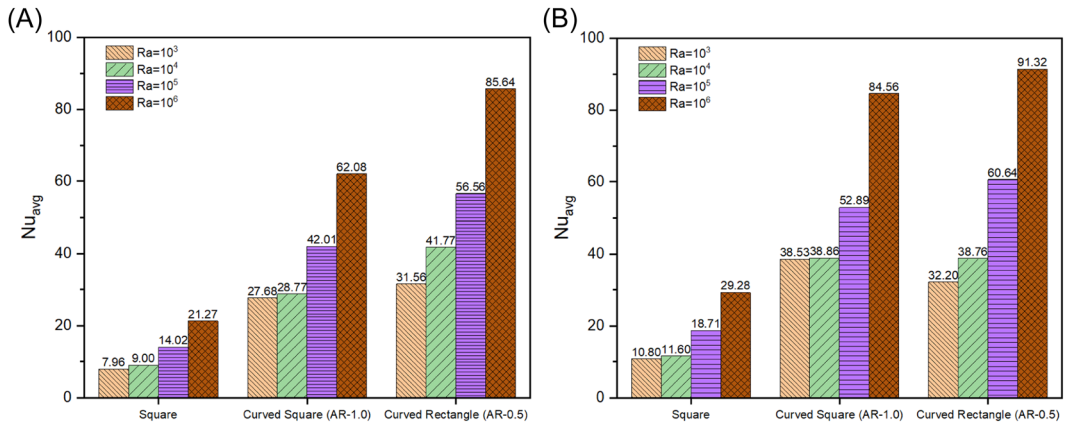

FIGURE 9 Variation of Nu_{avg} (A) without cooler and (B) with cooler for $Ra = 10^3$–10^6.

For each specific geometry, as the $|V|_{avg}$ increases, the Nu_{avg} also increases. Interestingly, in scenarios WC, it exhibits lower $|V|_{avg}$ than in the absence of a cooler. However, in cases WC, it demonstrates higher Nu_{avg}.

Table 3 provides data on various parameters, including S_{HT}, S_{FF}, En_{avg}, and Be_{avg} for two scenarios: WOC and WC, at different Ra ranging from 10^3 to 10^6 when $AR = 1.0$ and 0.5 S_{HT} is higher in the WOC case compared with WC at each Ra value. This suggests that the absence of a cooler results in more EG due to HT. Specifically, S_{HT} gradually increases from 0.5811 to 0.2615 for WOC and from 0.4139 to 0.1946 for WC as Ra increases. Similarly, S_{FF} exhibits a similar trend, with higher values in the WOC case at lower $Ra = 10^3$ and 10^4, but higher values in the WC case at higher $Ra = 10^5$ and 10^6. This implies that fluid friction contributes to higher EG, especially when a cooler is absent. The values of S_{FF} increase from 0.0013 to 28.2750 for WC and from 0.0005 to 32.5860 for WOC as Ra increases. The behavior of En_{avg} closely mirrors that of S_{FF}, with increasing values as Ra increases. With increasing Ra, the En_{avg} values rise from 0.5824 to 28.5365 for WOC and from 0.4143 to 32.7806 for WC. Finally, the Be_{avg} decreases

TABLE 3 Variation of S_{HT}, S_{FF}, S_{TL}, and Be for WC and WOC when $AR = 1.0$ and 0.5.

	10^3		10^4		10^5		10^6	
Ra	***WOC***	***WC***	***WOC***	***WC***	***WOC***	***WC***	***WOC***	***WC***
$AR = 1.0$								
S_{HT}	0.5811	0.4139	0.5892	0.4152	0.3862	0.3140	0.2615	0.1946
S_{FF}	0.0013	0.0005	0.1273	0.0508	2.8229	2.8232	28.2750	32.5860
En_{avg}	0.5824	0.4143	0.7165	0.4660	3.2091	3.1372	28.5365	32.7806
Be_{avg}	0.9977	0.9988	0.8223	0.8909	0.1203	0.1001	0.0092	0.0059
$AR = 0.5$								
S_{HT}	0.5111	0.5009	0.4251	0.4205	0.2851	0.2723	0.1844	0.1764
S_{FF}	0.0055	0.0048	0.2412	0.3009	3.9271	4.0469	38.5510	43.9160
En_{avg}	0.5166	0.5056	0.6664	0.7214	4.2122	4.3192	38.7354	44.0924
Be_{avg}	0.9893	0.9906	0.6185	0.5900	0.0677	0.0697	0.0048	0.0040

Abbreviations: AR, aspect ratio; WC, with a cooler; WOC, without a cooler.

as Ra increases for both cases. At Ra values of 10^3 and 10^4, Be_{avg} is greater than 0.5, indicating that S_{HT} dominates over S_{FF}. However, at higher Ra values (10^5 and 10^6), Be_{avg} is lower than 0.5, indicating that S_{FF} becomes more dominant than S_{HT}. The values of Be_{avg} decrease significantly from 0.9977 to 0.0092 for WOC and from 0.9988 to 0.0059 for WC as Ra increases.

For $AR = 0.5$, the behavior of S_{HT} follows similar trends as those observed for $AR = 0.5$. S_{HT} gradually increases from 0.5111 to 0.1844 for WOC and from 0.5009 to 0.1764 for WC as Ra increases. At $Ra = 10^3$, S_{FF} is higher in the WOC case compared with the WC case. However, for Ra values ranging from 10^4 to 10^6, S_{FF} is lower in the WOC case than in the WC case. The values of S_{FF} increase from 0.0055 to 38.5510 for WOC and from 0.0048 to 43.9160 for WC as Ra increases. This trend is also observed in En_{avg}. With increasing Ra, the En_{avg} values rise from 0.5166 to 38.7354 for WOC and from 0.5056 to 44.0924 for WC. Be_{avg} also follows a similar pattern, as for $AR = 1.0$. The values of Be_{avg} decrease significantly from 0.9893 to 0.0048 for WOC and from 0.9906 to 0.0040 for WC as Ra increases.

4.3 | Ecological Coefficient Performance (ECOP) for different shapes of geometry

Figure 10 illustrates the ECOP, represented as $\left(\frac{Nu_{avg}}{En_{avg}}\right)$ as Seyyedi et al.,[45] as it varies with the Ra ranging from 10^3 to 10^6 for different cavity shapes in two scenarios: WOC and WC. In Figure 10A, the highest ECOP is observed in the curved rectangle cavity for all Ra values, indicating that in the WOC case, this cavity shape enhances energy efficiency and reduces environmental impact compared with square and curved square cavities. Figure 10B shows that the curved square cavity exhibits the highest ECOP for all Ra values in the WC case. In the WC scenario, the curved square cavity improves energy efficiency and minimizes environmental impact compared with square and curved rectangle cavities. For both the WOC and WC cases,

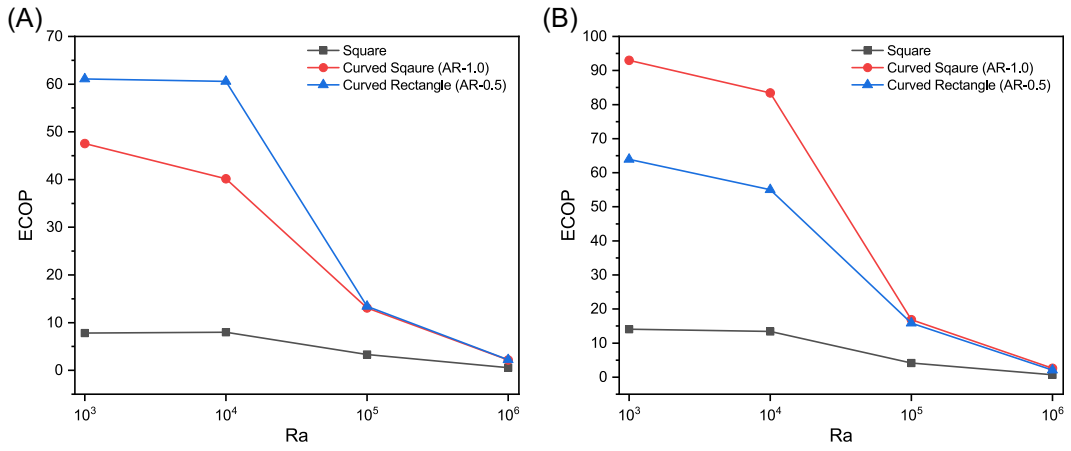

FIGURE 10 Variation of ECOP (A) without cooler and (B) with cooler for $Ra = 10^3$–10^6. AR, aspect ratio; ECOP, Ecological Coefficient Performance.

ECOP decreases with increasing *Ra*. This pattern implies that with rising *Ra* values, there could be a decrease in ECOP values, signifying a possible decline in energy efficiency and an escalation in the system's ecological footprint.

5 | CONCLUSION

The present study examined strategies for enhancing HT and EG analysis in a curved corner cavity while varying its AR and enclosing a circular shape cooler. The curved corner of the cavity has a noticeable effect on the HT properties of the system, leading to improved HT performance. This observation underscores the crucial role of the cavity's geometric configuration in shaping its impact on HT processes. The study's principal findings can be summarized as follows:

- In the case of WOC, Nu_{avg} is higher in the curved rectangle cavity ($AR = 0.5$) compared with the square and curved square cavities for all *Ra*.
- Using the curved square ($AR = 1.0$), Nu_{avg} increases by 191.86%, and with the curved rectangle ($AR = 0.5$), Nu_{avg} increases by 302.6% at $Ra = 10^6$.
- For the situation involving WC, Nu_{avg} surpasses that of WOC across all *Ra* values.
- Nu_{avg} and En_{avg} increase with *Ra* for both the WOC and WC cases.
- Transitioning from a square to a curved rectangle ($AR = 0.5$) WC, results in a 329.34% increase in Nu_{avg} at $Ra = 10^6$.
- The rise from 10^3 to 10^6 results in a reduction in energy efficiency and an increased environmental impact.
- The highest ECOP is observed in the curved rectangle cavity for all *Ra* values in the WOC case, indicating an increase in energy efficiency and a decrease in environmental impact.
- In the WOC case, the ECOP in the curved rectangle ($AR = 0.5$) is over six times higher than that in the square cavity at $Ra = 10^3$.
- In the WC case, the curved square cavity demonstrates the highest ECOP across all *Ra* values, signifying enhanced energy efficiency and reduced environmental impact.

The future prospects of this study could involve:

- This study covers *Ra* values from 10^3 to 10^6, but future research could explore even higher *Ra* values.
- Future work could investigate various cooler shapes for further insights.
- Future research could explore the effects of rotating coolers and the use of multiple coolers for a more comprehensive understanding.

NOMENCLATURE

Be	local Bejan number
Be_{avg}	average Bejan number
Da	Darcy number
EG	entropy generation
En_{avg}	total average entropy
k	thermal conductivity ($W m^{-2} K^{-2}$)
Le	Lewis number
P	dimensionless pressure
Pr	Prandtl number
q''	heat flux ($W m^{-2}$)
r	radius of the cooler (m)
Ra	Rayleigh number
Re	Reynolds number
Ri	Richardson number
S_{FF}	entropy generation due to fluid friction
S_{HT}	entropy generation due to heat transfer
S_{TL}	total local entropy
T_0	reference temperature (K)
T_c	cold temperature (K)
U	dimensionless horizontal velocity component
V	dimensionless vertical velocity component
$\lvert V\rvert_{avg}$	average velocity magnitude
X	dimensionless horizontal coordinate
Y	dimensionless vertical coordinate

GREEK SYMBOLS

α	thermal diffusivity of the base fluid ($m^2 s^{-1}$)
β_T	thermal expansion coefficient (K^{-1})
λ	irreversibility factor
μ	viscosity of the base fluid ($kg m^{-1} s^{-1}$)
ν	kinematic viscosity of the base fluid ($m^2 s^{-1}$)
ρ	density of fluid ($kg m^{-3}$)
Θ	nondimensional temperature of the fluid

ACKNOWLEDGMENTS

Jiaul Haque Saboj acknowledges NSU for supporting the R.A. ship under NSU CTRG research grant (Grant No. CTRG-22-SEPS-22). The Ministry of Science and Technology (MOST),

Government of the People's Republic of Bangladesh (Grant No. SRG-236670) is acknowledged for supporting the computational facility. Open access publishing facilitated by University of Technology Sydney, as part of the Wiley - University of Technology Sydney agreement via the Council of Australian University Librarians.

CONFLICT OF INTEREST STATEMENT

The authors declare no conflict of interest.

DATA AVAILABILITY STATEMENT

The data that support the findings of this study are available from the corresponding author upon reasonable request.

ORCID

Jiaul Haque Saboj http://orcid.org/0009-0008-2700-0146
Goutam Saha http://orcid.org/0000-0001-6467-298X
Suvash C. Saha http://orcid.org/0000-0002-9962-8919

REFERENCES

1. Ha MY, Kim I-K, Yoon HS, Lee S. Unsteady fluid flow and temperature fields in a horizontal enclosure with an adiabatic body. *Phys Fluids*. 2002;14(9):3189-3202.
2. Ha MY, Kim I-K, Yoon HS, et al. Two-dimensional and unsteady natural convection in a horizontal enclosure with a square body. *Numer Heat Transfer Part A*. 2002;41(2):183-210.
3. Lee JR, Ha MY, Balachandar S, Yoon HS, Lee SS. Natural convection in a horizontal layer of fluid with a periodic array of square cylinders in the interior. *Phys Fluids*. 2004;16(4):1097-1117.
4. Lee JR, Ha MY. Numerical simulation of natural convection in a horizontal enclosure with a heat-generating conducting body. *Int J Heat Mass Transfer*. 2006;49:2684-2702. doi:10.1016/j.ijheatmasstransfer.2006.01.010
5. Hyun JM, Lee JW. Numerical solutions for transient natural convection in a square cavity with different sidewall temperatures. *Int J Heat Fluid Flow*. 1989;10(2):146-151.
6. McBain G. Natural convection with unsaturated humid air in vertical cavities. *Int J Heat Mass Transfer*. 1997;40(13):3005-3012.
7. Ha MY, Jung MJ. A numerical study on three-dimensional conjugate heat transfer of natural convection and conduction in a differentially heated cubic enclosure with a heat-generating cubic conducting body. *Int J Heat Mass Transfer*. 2000;43(23):4229-4248.
8. Cheikh NB, Beya BB, Lili T. Influence of thermal boundary conditions on natural convection in a square enclosure partially heated from below. *Int Commun Heat Mass Transfer*. 2007;34(3):369-379.
9. Ikram MM, Saha G, Saha SC. Second law analysis of a transient hexagonal cavity with a rotating modulator. *Int J Heat Mass Transfer*. 2024;221:125039.
10. Saha T, Saha G, Parveen N, Islam T. Unsteady magneto-hydrodynamic behavior of TiO_2–kerosene nanofluid flow in wavy octagonal cavity. *Int J Thermofluids*. 2024;21:100530.
11. Saha G, Al-Waaly AA, Ikram MM, Bihani R, Saha SC. Unveiling the dynamics of entropy generation in enclosures: a systematic review. *Int J Thermofluids*. 2024;21:100568. doi:10.1016/j.ijft.2024.100568
12. Saha BK, Jihan JI, Ahammad MZ, Saha G, Saha SC. Enhanced thermal performance and entropy generation analysis in a novel cavity design with circular cylinder. *Heat Transfer*. 2024. doi:10.1002/htj.22999
13. Saha G, Al-Waaly AA, Paul MC, Saha SC. Heat transfer in cavities: configurative systematic review. *Energies*. 2023;16(5):2338.
14. Ikram MM, Saha G, Saha SC. Unsteady conjugate heat transfer characteristics in hexagonal cavity equipped with a multi-blade dynamic modulator. *Int J Heat Mass Transfer*. 2023;200:123527.
15. Ikram MM, Saha G, Saha SC. Conjugate forced convection transient flow and heat transfer analysis in a hexagonal, partitioned, air filled cavity with dynamic modulator. *Int J Heat Mass Transfer*. 2021;167:120786.

16. Natarajan E, Roy S, Basak T. Effect of various thermal boundary conditions on natural convection in a trapezoidal cavity with linearly heated side wall (s). *Numer Heat Transfer Part B*. 2007;52(6):551-568.
17. Corvaro F, Paroncini M. A numerical and experimental analysis on the natural convective heat transfer of a small heating strip located on the floor of a square cavity. *Appl Therm Eng*. 2008;28(1):25-35.
18. Varol Y, Oztop HF, Yilmaz T. Two-dimensional natural convection in a porous triangular enclosure with a square body. *Int Commun Heat Mass Transfer*. 2007;34(2):238-247.
19. Hussein AK, Hussain SH. Numerical analysis of steady natural convection of water in inclined square enclosure with internal heat generation. In: *2010 International Conference on Mechanical and Electrical Technology*. IEEE; 2010:502-508. doi:10.1109/ICMET.2010.5598412
20. Saglam M, Sarper B, Aydin O. Natural convection in an enclosure with a pair of discrete heat sources. *J Thermophys Heat Transfer*. 2019;33(1):234-245.
21. Rabani M. Impact of cavity chord shape on the free convection heat transfer rate in a triangular cavity. *Heat Transfer—Asian Res*. 2019;48(7):2909-2929.
22. Saleem KB, Alshara AK. Natural convection in a triangular cavity filled with air under the effect of external air stream cooling. *Heat Transfer–Asian Res*. 2019;48(7):3186-3213.
23. Alipanah M, Ranjbar A, Farnad E, Alipanah F. Entropy generation of natural convection heat transfer in a square cavity using Al_2O_3–water nanofluid. *Heat Transfer–Asian Res*. 2015;44(7):641-656.
24. Shu C, Zhu Y. Efficient computation of natural convection in a concentric annulus between an outer square cylinder and an inner circular cylinder. *Int J Numer Methods Fluids*. 2002;38(5):429-445.
25. Angeli D, Levoni P, Barozzi GS. Numerical predictions for stable buoyant regimes within a square cavity containing a heated horizontal cylinder. *Int J Heat Mass Transfer*. 2008;51(3-4):553-565.
26. Xu X, Yu Z, Hu Y, Fan L, Cen K. A numerical study of laminar natural convective heat transfer around a horizontal cylinder inside a concentric air-filled triangular enclosure. *Int J Heat Mass Transfer*. 2010;53(1-3):345-355.
27. Kim B, Lee D, Ha M, Yoon H. A numerical study of natural convection in a square enclosure with a circular cylinder at different vertical locations. *Int J Heat Mass Transfer*. 2008;51(7-8):1888-1906.
28. Chowdhury R, Khan MAH, Siddiki MA. Natural convection in porous triangular enclosure with a circular obstacle in presence of heat generation. *Am J Appl Math*. 2015;3(2):51-58.
29. Ali ME-S, Nuhait AO, Alabdulkarem A, Almuzaiqer R. Free convection heat transfer inside square water-filled shallow enclosures. *PLoS ONE*. 2018;13(10):e0204251.
30. Welhezi H, Ben-Cheikh N, Ben-Beya B. Numerical analysis of natural convection between a heated cube and its spherical enclosure. *Int J Therm Sci*. 2020;150:105828.
31. Saboj JH, Nag P, Saha G, Saha SC. Entropy production analysis in an octagonal cavity with an inner cold cylinder: a thermodynamic aspect. *Energies*. 2023;16(14):5487.
32. Arquis E, Rady M. Study of natural convection heat transfer in a finned horizontal fluid layer. *Int J Therm Sci*. 2005;44(1):43-52.
33. Dou H-S, Jiang G, Zhang L, et al. A numerical study of natural convection heat transfer in fin ribbed radiator. *Math Probl Eng*. 2015;2015:1-13. doi:10.1155/2015/989260
34. Taloub D, Bouras A, Djezzar M, Driss Z. Numerical research of double-diffusive natural convection in elliptical cylinders: effect of thermal Rayleigh number. *Heat Transfer*. 2020;49(4):2194-2205.
35. Khan ZH, Khan WA, Elbaz AM, Qasim M, Alharbi SO, Sun L. Natural convection in triangular fin-shaped cavity with partially heated base using nanofluid. *ZAMM—J Appl Math Mech/Z Angew Math Mech*. 2021;101(12):e202000306.
36. Biswas N, Mandal DK, Manna NK, Benim AC. Magneto-hydrothermal triple-convection in a W-shaped porous cavity containing oxytactic bacteria. *Sci Rep*. 2022;12(1):18053.
37. Mandal DK, Biswas N, Manna NK, Gorla RSR, Chamkha AJ. Hybrid nanofluid magnetohydrodynamic mixed convection in a novel W-shaped porous system. *Int J Numer Meth Heat Fluid Flow*. 2023;33(2):510-544.
38. Mandal DK, Biswas N, Manna NK, Gayen DK, Gorla RSR, Chamkha AJ. Thermo-fluidic transport process in a novel M-shaped cavity packed with non-Darcian porous medium and hybrid nanofluid: Application of artificial neural network (ANN). *Phys Fluids*. 2022;34(3):033608. doi:10.1063/5.0082942
39. Mandal DK, Biswas N, Manna NK, Gorla RSR, Chamkha AJ. Role of surface undulation during mixed bioconvective nanofluid flow in porous media in presence of oxytactic bacteria and magnetic fields. *Int J Mech Sci*. 2021;211:106778.

40. Al-Farhany K, Alomari MA, Saleem KB, Al-Kouz W, Biswas N. Numerical investigation of double-diffusive natural convection in a staggered cavity with two triangular obstacles. *Eur Phys J Plus*. 2021;136(8):814.
41. Saha G, Saha S, Hasan MN, Islam Q. Natural convection heat transfer within octagonal enclosure. *IJE Trans A*. 2010;23(1):1-10.
42. Ilis GG, Mobedi M, Sunden B. Effect of aspect ratio on entropy generation in a rectangular cavity with differentially heated vertical walls. *Int Commun Heat Mass Transfer*. 2008;35(6):696-703.
43. Sivaraj C, Sheremet M. MHD natural convection and entropy generation of ferrofluids in a cavity with a non-uniformly heated horizontal plate. *Int J Mech Sci*. 2018;149:326-337.
44. Mussa M, Abdullah S, Azwadi CN, Muhamad N. Simulation of natural convection heat transfer in an enclosure by the lattice-Boltzmann method. *Comput Fluids*. 2011;44(1):162-168.
45. Seyyedi MS, Rajaee-Zadeh T, Hashemi-Tilehnoee M. A new model to measure the performance of the fins based on exergy analysis. *Therm Sci*. 2019;23(2 Part A):509-523.

How to cite this article: Saboj JH, Nag P, Saha G, Saha SC. Heat transfer assessment incorporated with entropy generation within a curved corner structure enclosing a cold domain. *Heat Transfer*. 2024;53:2460-2479. doi:10.1002/htj.23044